Final Draft

of the original manuscript

Itzhak, T.; Segev-Mark, N.; Simon, A.; Abetz, V.; Ramon, G.; Segal-Peretz, T.:

Atomic Layer Deposition for Gradient Surface Modification and Controlled Hydrophilization of Ultrafiltration Polymer Membranes.

Atomic Layer Deposition for Gradient Surface Modification and Controlled Hydrophilization of Ultrafiltration Polymer Membranes

Tamar Itzhak, Naama Segev-Mark, Assaf Simon, Volker Abetz, Guy Z. Ramon, and Tamar Segal-Peretz*

ABSTRACT: In recent years, atomic layer deposition (ALD) has emerged as a powerful technique for polymeric membrane surface modification. In this research, we study Al_2O_3 growth via ALD on two polymeric phase inverted membranes: polyacrylonitrile (PAN) and polyetherimide (PEI). We demonstrate that Al_2O_3 can easily be grown on both membranes with as little as 10 ALD cycles. We investigate the formation of Al_2O_3 layer gradient through the depth of the membranes using high resolution transmission electron microscopy and elemental analysis, showing that at short exposure times, Al_2O_3 accumulates at the top of the membrane, reducing pore size and creating a strong growth gradient, while at long exposure time, more homogeneous growth occurs. This detailed characterization creates the knowledge necessary for controlling

Increase in exposure time

the deposition gradient and achieving an efficient growth with minimum pore clogging. By tuning the Al_2O_3 exposure time and cycles, we demonstrate control over the Al_2O_3 depth gradient and membranes' pore size, hydrophilicity, and permeability. The oil antifouling performance of membranes is investigated using *in situ* confocal imaging during flow. This characterization technique reveals that Al_2O_3 surface modification reduces oil droplet surface coverage.

KEYWORDS: *atomic layer deposition, membranes, ultrafiltration, oxide, gradient, transmission electron microscopy*
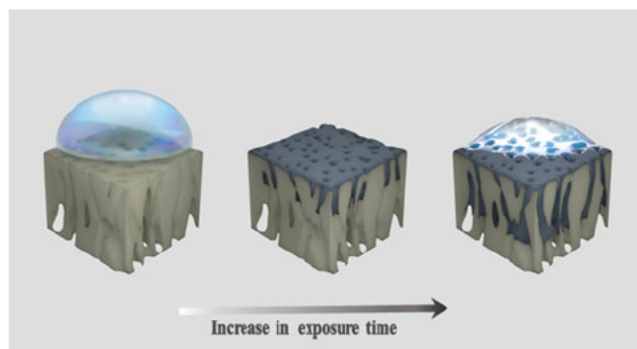
1. INTRODUCTION

Surface modifications are commonly used practices in membrane fabrication to enhance membrane performance.[1−3] Surface modification methods such as polymer or additive incorporation within the membrane matrix,[4−8] chemical reactions on the as cast or prepared membrane,[9−12] and grafting or coating with various materials have been shown to improve membrane properties including membrane hydro philicity, permeability, selectivity, and antifouling.[13−19] In the last several years, atomic layer deposition (ALD) has emerged as a powerful technique for membrane surface and pore network modification due to its ability to grow thin inorganic coatings on the walls of the tortuous porous network with sub nanometer precision of the coating thickness.[14,20−28] ALD is based on sequential exposure of two gas phase precursors, creating thin films, one atomic layer at a time, allowing precise control over the growth process in a wide array of inorganic materials.[29] Conformal coating of metal oxides on the outer and inner pore surfaces by ALD has been demonstrated in microfiltration (MF) and ultrafiltration (UF) membranes and recently in nanofiltration (NF) and reverse osmosis (RO) membranes as well.[30,31] With judicious choice of materials and growth conditions, the metal oxide coatings can be harnessed to tune pore structure and pore surface properties, with emphasis on improving surface hydrophilicity and its resistance to fouling.

Most past studies on ALD on membranes utilized ALD growth as a uniform surface modification method within the inner pore system or have concentrated on the pore structure at the top of the membrane. While ALD is an ideal technique for thin film deposition on high aspect ratio structures, ALD growth on polymer surfaces is not necessarily uniform across the membranes' depth, especially in the tight pore systems of UF−NF membranes. This nonuniformity can occur both in reactive polymers such as poly(ether sulfone) (PES) and polyimide (PI),[32,33] where ALD nucleation can easily take place, as well as in inert polymers such as poly(vinylidene fluoride) (PVDF) and polypropylene (PP) where ALD nucleation is challenging.[14,25] Indeed, recent studies started to explore the precursors' exposure time (time allowed for the precursors to diffuse and chemisorb on the substrate surface) needed to achieve significant growth on membranes.[28,30,31]

However, while uniform in depth pore surface modification is usually sought after, the ability to control and tune the growth depth can open new pathways to engineer membranes' properties.[34] For example, Darling et al. have fabricated Janus membranes with hydrophilic and hydrophobic top and bottom surfaces by creating a gradient in Al_2O_3 growth on hydrophobic PP membranes.[35] It is therefore desired to investigate in detail gradient formation in ALD on polymer membranes and its effect on the performance of membranes.

To understand ALD gradients in polymer membranes, reactive polymers where nucleation and growth of metal oxides can easily be performed on their surface provide a good model system. In many hydrophobic polymers such as PVDF and PP, the inert surface hinders ALD growth.[30,32,36,37] Thus, extensive numbers of ALD cycles or pre ALD treatment steps such as oxygen plasma and surface sensitization[38] are needed to promote ALD nucleation and growth. To create a simple correlation between the ALD process and the formed gradient, polyacrylonitrile (PAN) and polyetherimide (PEI) were chosen as polymer model systems due to their nitrile (PAN), ether, and imide (PEI) groups in the polymers' backbone, which can provide reactive moieties for organometallic precursor adsorption and ALD growth. These membranes, to the best of our knowledge, have not been explored yet as the basis for ALD modifications.

In this research, we investigate the growth of Al_2O_3 as a model system on PAN and PEI phase inverted asymmetric membranes using ALD and study Al_2O_3 gradient formation in these membranes by direct imaging with high resolution transmission electron microscopy (HR TEM) and elemental analysis with TEM energy dispersive spectroscopy (EDS). We aim to shed light on the effect of exposure time on Al_2O_3 growth and the consequent shift in membrane permeability to better understand how to reach improved hydrophilicity and membrane performance while maintaining an efficient ALD process and preventing pore clogging in UF membranes. Following exposure time optimization, we explore Al_2O_3 growth on these polymer surfaces that are highly favorable for nucleation and the resulting structure and membrane properties. To probe oil antifouling behavior of the modified membranes, we perform *in situ* confocal microscopy imaging to characterize the oil coverage on the membranes' surface.

2. MATERIALS AND METHODS

2.1. UF Membranes. The polymer UF membranes were prepared using nonsolvent induced phase inversion (NIPS). Commercial grade PAN and PEI were dissolved in organic solvents and cast on a commercially available polyester nonwoven using a homemade casting machine. After a specific period of time, the membranes were immersed in water to induce the solvent−nonsolvent exchange, leading to an integral asymmetric morphology. They were subsequently washed and dried to remove residual solvent prior to further use.

2.2. ALD Process. ALD processes were performed in Veeco Savannah S100 using trimethylaluminum (TMA, Strem Chemicals, Inc.) and H_2O. The membranes were placed in the ALD chamber at 95 °C. The chamber was then heated to 100 °C and stabilized for at least 10 min before starting the process under 20 sccm N_2 flow and at 0.3 Torr base pressure. Each ALD cycle consists of (1) TMA pulse (0.015 s), (2) exposure step, allowing the precursor time to diffuse and interact with the membrane's surface, (3) chamber purge, and (4−6) where steps (1)−(3) are performed with H_2O.

2.3. Structural Characterization and Elemental Analysis. Al_2O_3 growth was probed using energy dispersive X ray spectroscopy (EDS, Bruker) system coupled to a high resolution scanning electron microscope (SEM) with a field emission gun (Zeiss Ultra Plus). The EDS analysis was performed at 4 kV acceleration voltage, with 8 mm working distance and 300 s dwell time. SEM imaging was performed at a 1 kV acceleration voltage, with 3.8−4.8 mm working distance. For imaging, the specimens were coated with 3 nm iridium to reduce specimen charging. Image analysis of the pore size was performed using the pore size distribution code in MATLAB.[39]

Al_2O_3 depth profiling was performed using transmission electron microscopy (TEM, Thermo Fisher Talos 200C) bright field image series. Cross sectional specimens for TEM imaging were prepared by infiltrating epoxy resin into the membrane. After epoxy solidification, the membrane samples were sliced with a microtome (Ultra microtome Leica EM UC7) to 70 nm thick slices. Scanning transmission electron microscopy (STEM) EDS imaging and analysis were performed using Thermo Fisher Titan Cubed Themis G2 60−300, operated at 200 kV. Each EDS line scan was acquired using 30 min acquisition time. To compare between specimens having different ALD exposure times, we normalized the Al intensity measured by STEM EDS to the carbon intensity, which is equal between specimens with the same membrane type. The carbon intensity was averaged using three different measurements in each exposure time. Finally, the Al curve was also normalized to one.

2.4. Membrane Characterization. Dynamic water contact angle (CA) measurements were performed by a goniometer (Data Physics; OCA 15Pro) using the advancing−receding technique. In each measurement, a 5 μL drop of deionized water was dripped on the membrane surface and the average between the advancing and receding angles was calculated. Each contact angle measurement was repeated three times.

Water permeability measurements were performed in a dead end filtration stirred cell (Amicon Stirred Cells, UFSC05001, 50 mL) at room temperature with double distilled water. The water perme ability, L_P, was calculated using

$$L_p = \frac{V}{At\Delta P} \tag{1}$$

where A (m^2) is the effective filtration area, t (h) is the duration between two measurements (30 s), V (L) is the permeate volume accumulated during the time, and ΔP (bar) is the transmembrane pressure (TMP). The water permeability was measured at a transmembrane pressure of 3 bar for PEI membranes and 1 bar for PAN membranes. Each membrane was prewetted before the measurements. The hydrophobic PEI membranes were prewetted with 50% ethanol in water solution for several seconds to promote wetting, followed by 1 h prewetting in water. The hydrophilic PAN membranes were directly wetted by immersing them in water for 1 h.

The membrane pore diameter (r_p) was estimated from the membrane permeability, L_p, using the Hagen−Poiseuille equation for flow through tortuous pores[40,41]

$$L_p = \frac{br_p^2 \varnothing}{\mu \alpha \Delta x} \tag{2}$$

where L_p (L/(m^2 h bar)) is the measured water permeability, μ (Pa s) is the water viscosity, Δx (μm) is the thickness of the membrane active layer, α is the tortuosity factor, $\varnothing$ is the membrane porosity, and $b = 1/8$ for random pores. α values were estimated by the membrane porosity according to the random pores model.[41] Δx and $\varnothing$ values were measured by image analysis of cross sectional and top down SEM images, respectively.

2.5. Direct Observation of Oil Droplet Deposition and Removal. *In situ* imaging filtration experiments were conducted using PEI and PAN membranes with and without the Al_3O_2 ALD layer. Membranes subjected to 10 cycles of Al_2O_3 ALD were chosen for the *in situ* imaging filtration characterization to enable direct comparison of the surface chemistry effect on oil fouling with minimum pore morphology changes.

2.5.1. Experimental System. The experimental setup is shown schematically in Figure 1. A custom made crossflow filtration cell, with a sapphire glass viewing port, allows *in situ* observation using a
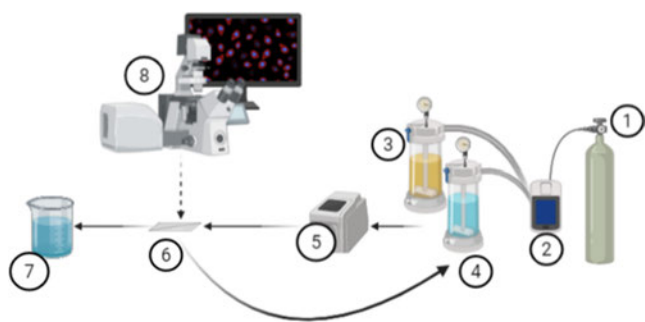
Figure 1. *In situ* imaging filtration system scheme: (1) compressed air, (2) pressure flow rate controller, (3) feed vessel (emulsion), (4) feed vessel (DI water), (5) gear pump, (6) flow cell, (7) permeate vessel, and (8) confocal microscope.

confocal laser scanning microscope (TCS SP8, Leica Micro systems).[42−47] Channel dimensions within the cell are 0.6 mm (H), 6 mm (W), and 36 mm (L) with a total membrane filtration area of 216 mm². The flow cell was mounted on the microscope stage, and imaging was made with a 25× water immersion objective with a numerical aperture of 0.95, corresponding to a 262 144 pixel (384 400 μm²) field of view. Experiments were carried out at room temperature (22 °C) and pH 6 (unadjusted). The filtration cell was supplied with emulsion by a gear pump, from a pressurized feed vessel. A software based pressure controller (Fluigent Maesflow 3.3.1) was used to fix the permeate flow rate while measuring the corresponding trans membrane pressure (TMP). The feed vessel was stirred at 400 rpm using a magnetic stirrer plate.

2.5.2. Feed Solution. The feed oil emulsion comprised 0.3 mM (77.2 mg/L) hexadecane, 0.02 mM surfactant Triton X 100, and 10 mM sodium chloride in DI water. Hexadecane was first stained with 1% Dye Lite (fluorescent dye, excitation@561 nm) and then mixed with water using a homogenizer for 3 min at 11 000 rpm, followed by surfactant addition.

2.5.3. Deposition and Cleaning Experiments. Filtration experiments were performed at a constant flux of 300 L/(m² h) (LMH) and included two stages: (1) first 20 min, deposition of oil droplets at the fixed flux in dead end operation, during which five random images of the membrane surface at different locations were acquired every 5 min and (2) cleaning, 10 min of crossflow flushing, using water with no permeation through the membrane ($J_w = 0$).

3. RESULTS AND DISCUSSION

3.1. Al$_2$O$_3$ ALD on PAN and PEI Membranes. We start with investigating Al$_2$O$_3$ growth on PEI and PAN membranes to enable control over the pore structure and surface chemistry. PAN membranes have a cross sectional morphology consisting of a dense layer at the top supported by fingerlike macrovoids in the substructure (Figure 2a) and an average pore diameter of 16 ± 4 nm on the top surface (Figure 2c), while PEI membranes have a cross sectional morphology of a dense layer supported by a spongelike substructure (Figure 2b), with an average pore diameter of 21 ± 11 nm on the top surface (Figure 2f).

We performed Al$_2$O$_3$ ALD using a TMA exposure time of 10 s to allow TMA penetration into the membranes' tortuous pore network. Interestingly, already at 10 Al$_2$O$_3$ ALD cycles, Al$_2$O$_3$ growth was observed in both membranes as can be seen from the reduction in pore size (Figure 2i) based on top down SEM as well as from EDS analysis (Figure 2j,k). This indicates that, as hypothesized, both PEI and PAN membranes are excellent substrates for Al$_2$O$_3$ ALD; the interactions between the polymer moieties and TMA enable fast nucleation and growth on the polymer membrane surface. As can be expected,

an increase in the number of ALD cycles results in a decrease in pore size, with pore size reduced from 21 ± 11 nm in pristine PEI membranes to 10 ± 4 nm after 100 Al$_2$O$_3$ ALD cycles and from 16 ± 4 nm in pristine PAN membranes to 6 ± 1 nm after 100 Al$_2$O$_3$ ALD cycles. In addition, the total membrane porosity also decreases with cycles (Figure S1) due to pore size reduction as well as blockage of the pores smaller than the average sized pores.

To gain further insights into the Al$_2$O$_3$ growth, we performed top down SEM EDS characterization (Figures 2j,k and S2). The analysis shows that in both membranes there is a linear increase in Al content in the membranes with Al$_2$O$_3$ ALD cycles; this increase reaches a plateau after 70 cycles in the PAN membrane, while in PEI membranes, it plateaus after 50 cycles. In the first 50−70 cycles, Al$_2$O$_3$ is grown on the pore walls by diffusing within the tortuous pore network of the membranes, resulting in a continuous increase in the Al content with depth. On the other hand, for a higher number of ALD cycles, above 50−70 cycles, the pore diameter is reduced by ∼10 nm or more, resulting in partial pore blockage, shifting the growth to the surface of the membranes, significantly reducing the growth rate. In addition, a high Al content can reduce the penetration depth of the electron beam during EDS characterization, resulting in a lower EDS signal, contributing to the plateau.

3.2. Control over Al$_2$O$_3$ Gradient Growth. With our understanding of Al$_2$O$_3$ growth on PEI and PAN membranes, we turn to investigate the effect of exposure time on Al$_2$O$_3$ growth and Al$_2$O$_3$ gradient formation using high resolution cross sectional TEM. Here, we set the number of cycles to 30, which demonstrated significant Al$_2$O$_3$ growth but was sufficiently low so as to prevent pore clogging (Figures 2 and S2). Figure 3 presents bright field imaging of a microtome sliced PEI membrane with 30 cycles of Al$_2$O$_3$ ALD with 0.1 and 60 s TMA exposure times. The H$_2$O exposure time was kept constant at 10 s. In these images, the dark connected matrix corresponds to the PEI membrane, bright domains correspond to the embedded epoxy, and the thin black layers correspond to the Al$_2$O$_3$ coating as marked in Figure 3b 1. The full view of the membrane cross section, where all of the cross sectional images are joined together, is presented in Figure S3.

We estimated the Al$_2$O$_3$ growth depth by observing the Al$_2$O$_3$ layer contrast. Even with a short exposure time of 0.1 s, Al$_2$O$_3$ growth was observed deep within the internal pores (Figure 3a), up to a depth of 5.8 ± 0.4 μm. Upon increasing the exposure time to 60 s, Al$_2$O$_3$ grew deeper within the membrane, to an average growth depth of 9.9 ± 0.4 μm. PAN membranes showed similar behavior with an average growth depth of 5.5 ± 0.6 and 10.1 ± 1.2 μm for 0.1 and 60 s, respectively (Figure S4). The nanometric scale pores of UF membranes enable small ALD precursors such as TMA and H$_2$O to diffuse deeply into the pores and coat the high aspect ratio structure of the tortuous pore network. This is in contrast to reverse osmosis membranes and nanofiltration membranes where the sub nanometer pore size limits precursor diffusion into the membrane.[31] Nonetheless, the growth depth is diffusion limited; hence, increased exposure time leads to deeper penetration and growth. When comparing the growth depth in these UF membranes, we observed that even at an extremely long exposure time of 60 s, the growth depth was smaller than that in previously reported Al$_2$O$_3$ ALD coatings on inorganic, high aspect ratio structures such as anodic alumina (AA) membranes, where 20−50 μm growth depths
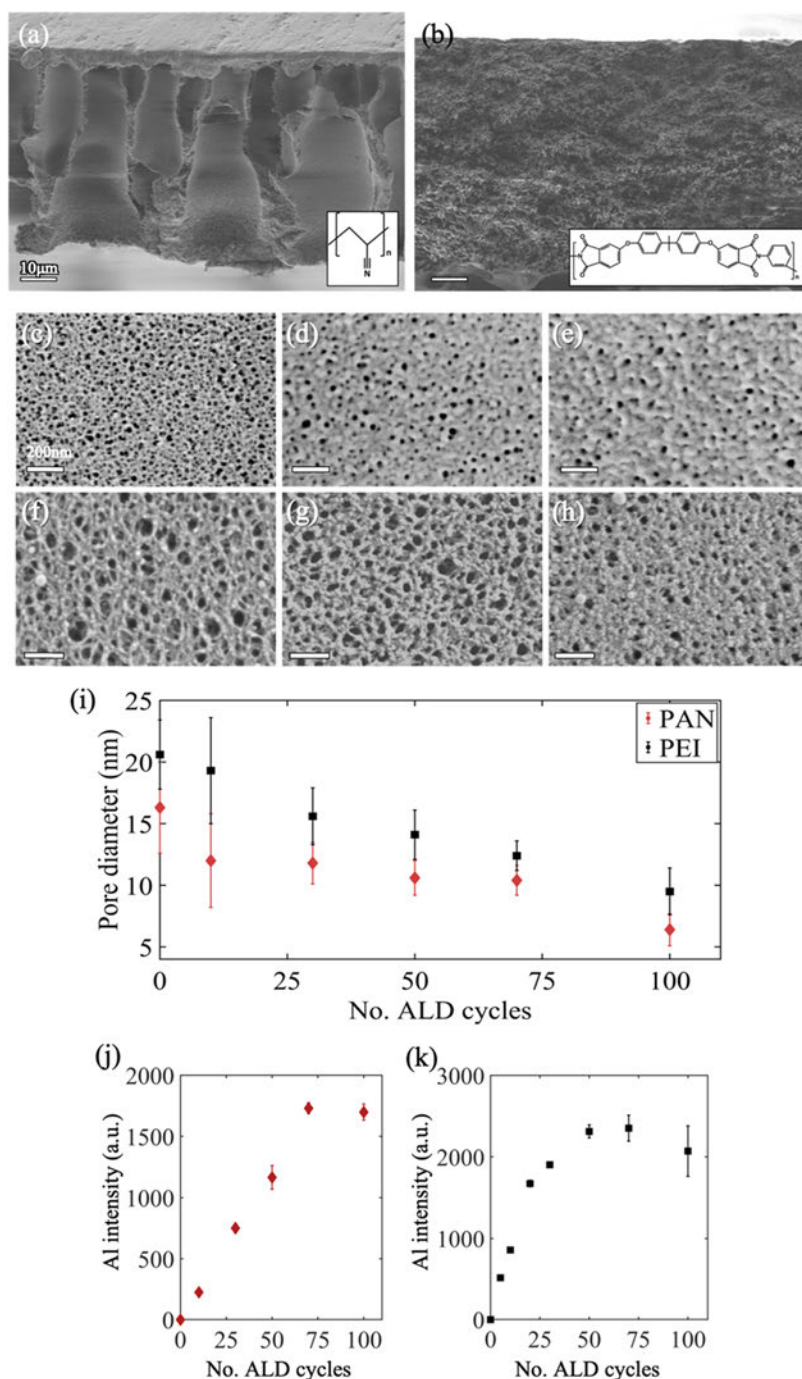
Figure 2. Al$_2$O$_3$ ALD on PAN and PEI membranes: (a, b) cross sectional SEM images and their corresponding chemical structures (inset) of PAN and PEI, respectively. Top down SEM images of (c−e) PAN and (f−h) PEI membranes: (c, f) pristine, (d, g) after 30 cycles of Al$_2$O$_3$ ALD, and (e, h) after 70 cycles of Al$_2$O$_3$ ALD. (i) Pore diameter as a function of Al$_2$O$_3$ ALD cycles, measured from top down SEM images. (j, k) Al Kα intensity in SEM EDS spectra of PAN and PEI membranes, respectively.

were observed.[48,49] These differences might be due to the variations in the aspect ratio, which are difficult to measure in polymer membranes with their nonuniform pore size and tortuous pore paths, or due to the precursor−polymer wall interactions at the nucleation stage, which can be different than inorganic surfaces such an AA surface.

In addition to growth depth, the exposure time affects the Al$_2$O$_3$ layer thickness and its gradient across the membrane. At a short exposure time of 0.1 s, there is higher Al$_2$O$_3$ growth at the top of the membrane, as can be seen by the darker contrast in Figure 3a 1 (white arrow), compared to the uniform Al$_2$O$_3$

layer at the top of the membrane with a 60 s exposure time (Figure 3b 1). High magnification TEM imaging (Figure 4) reveals that this higher Al$_2$O$_3$ growth at a short exposure time results in a thicker Al$_2$O$_3$ layer (3.1 ± 0.5 nm) at the top of the membrane, compared to Al$_2$O$_3$ thickness of 2.1 ± 0.5 nm with a 60 s exposure time. The penetration depths and layer thicknesses measured from the HR TEM images are summarized in Table 1. The variation between the growth at the top of the membrane and that within the membrane substructure at a short exposure time indicates that the precursors lack sufficient time to diffuse into the pore network
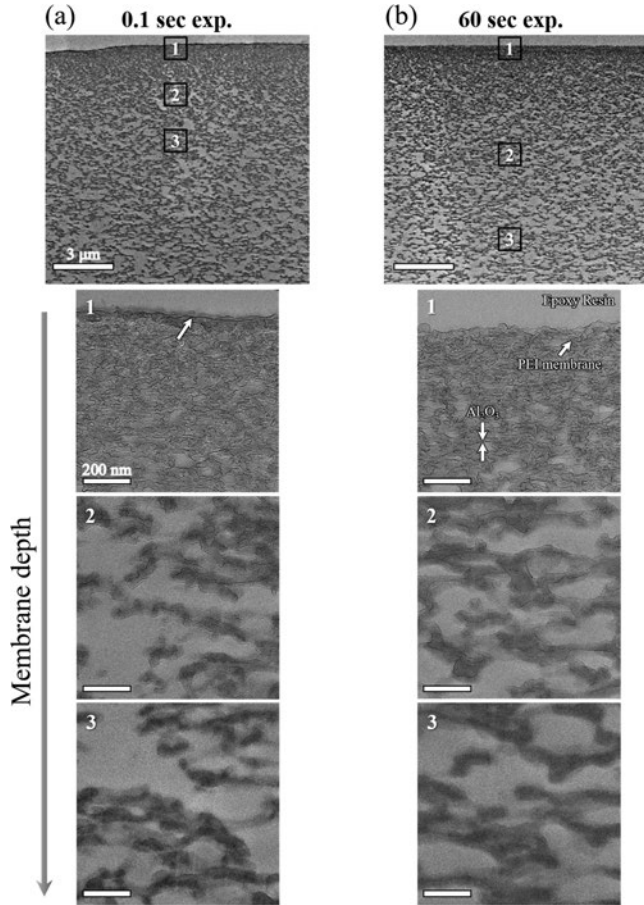
Figure 3. Al$_2$O$_3$ growth on PEI membranes: microtome cross sectional TEM images of the PEI membrane after 30 cycles of Al$_2$O$_3$ TMA ALD with (a) 0.1 s exposure time and (b) 60 s exposure time.

Table 1. Al$_2$O$_3$ ALD Penetration Depth in PAN and PEI Membranes and the Formed Layer Thickness at the Top Membrane Surface with Varying ALD Exposure Times

	PAN membrane		PEI membrane	
exposure time (s)	penetration depth (μm)	Al$_2$O$_3$ layer thickness (nm)	penetration depth (μm)	Al$_2$O$_3$ layer thickness (nm)
0.1	5.5 ± 0.6	3.5 ± 0.6	5.8 ± 0.4	3.1 ± 0.5
60	10.1 ± 1.2	2.7 ± 0.5	9.9 ± 0.4	2.1 ± 0.4

PEI membranes. A clear gradient in the Al signal is seen in both 0.1 and 60 s exposure membranes (Figure 5a,b,
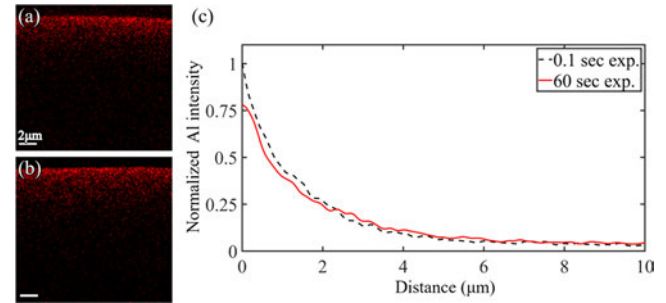
Figure 5. STEM EDS analysis of PEI membranes after 30 cycles of Al$_2$O$_3$ ALD with (a) 0.1 s and (b) 60 s exposure times. (c) Line scan analysis of the normalized Al intensity as a function of distance from the membrane top surface.

respectively), with high Al content at the top of the membrane, which decreases with depth. To compare the gradient between the membranes, the Al EDS counts were normalized with respect to the carbon counts as the carbon content is equal in both specimens (see Section 2.3 for additional details). The comparison between the Al EDS intensities (Figure 5c) showed that indeed Al$_2$O$_3$ growth with 0.1 s exposure resulted in high Al content at the top of the membrane compared to the membrane with 60 s exposure, in agreement with the bright field imaging discussed in Figures 3 and 4. The Al gradient, however, differs between STEM EDS characterization and bright field imaging characterization. The EDS analysis showed a decaying Al content in both membranes, reaching the noise level at a depth of ~5 μm, with a higher Al content at the 0.1 s exposure membrane at the first 2 μm underneath the membrane surface compared to the 60 s exposure. In the bright field imaging (Figure 3), on the other hand, no significant difference between the membranes was observed within the first 2 μm, but 60 s exposure membranes showed an almost doubled penetration depth compared with the 0.1 s

and interact homogeneously with the polymer on the pore walls. Interestingly, the relatively homogeneous growth at a high exposure time results in growth rate equivalent to Al$_2$O$_3$ ALD growth at 100 °C on flat Si/SiO$_2$ substrates, measured in our system (0.9 Å/cycle), indicating nearly ideal nucleation on the polymeric surface. It is important to note that the growth rate observed by TEM is higher than the rate observed from top down SEM analysis (~0.55 Å/cycle, Figure 2i). We attribute this difference to the different interaction of the specimen with the electron beam and the detecting systems in the two imaging platforms.[34]

To further characterize the Al$_2$O$_3$ gradient within the membranes, we performed STEM EDS elemental mapping of
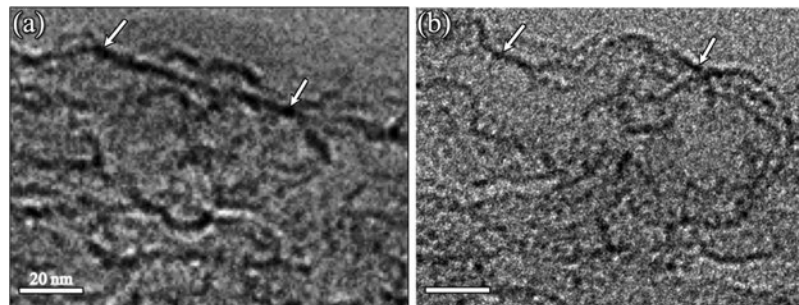

Figure 4. High resolution TEM images of the PEI membrane after 30 cycles of TMA ALD with (a) 0.1 s exposure time and (b) 60 s exposure time. White arrows show examples of the Al$_2$O$_3$ layer at the top of the membrane.

exposure membranes. While EDS characterization is based on X ray emission from Al atoms, the bright field imaging analysis is based on mass thickness contrast. Thus, bright field imaging is less sensitive to the Al content gentle decay but can identify the presence of an extremely thin Al_2O_3 layer, which gives low intensity in the EDS characterization.

With our understanding of the role of exposure time in the Al_2O_3 nanoscale growth in PEI and PAN membranes, built through STEM EDS and bright field imaging complementary characterizations, we explored how the exposure time affects the performance of macroscopic membranes, i.e., the membranes' water permeability. A PEI membrane was chosen as a model system, and the normalized permeability of PEI–Al_2O_3 membranes with varying ALD exposure times is presented in Figure 6. With an increase in the exposure
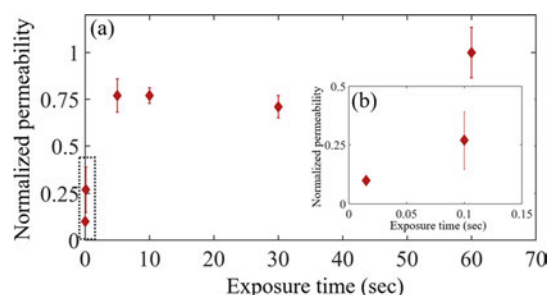

Figure 6. (a) Normalized water permeability as a function of the process exposure time of PEI membranes after 30 cycles of Al_2O_3 ALD. (b) Magnification of the first two points.

time, the permeability increased, reaching a plateau in membranes with 5 s TMA exposure time or longer. In short exposure time, a significant layer of Al_2O_3 is grown at the top of the membrane, causing blockage of the membrane pores, thus leading to reduced water permeability. For longer exposure times, on the other hand, Al_2O_3 spreads more homogeneously across the membrane depth and such blockage does not exists, leading to higher permeability values.

3.3. Tuning Hydrophilicity and Permeability. ALD on membrane surfaces can be utilized to tune membrane

hydrophilicity.[25,36] We characterized the Al_2O_3 modified PEI and PAN membranes' surface wetting properties through advancing and receding contact angle (CA) measurements (Figure 7a).

To maintain high permeability together with process efficiency, we set the TMA exposure time to 10 s. The contact angle measurements were performed immediately after the ALD process to minimize the effects of humidity adsorption on the membrane. Pristine PEI membranes had a relatively hydrophobic surface with CA of 65° (Figure 7a,b). Ten cycles of Al_2O_3 ALD significantly reduced the CA to 40°, with additional cycles further reducing it to a level of 20° at 50 cycles and onward, creating a hydrophilic surface (Figure 7c). Pristine PAN membranes, on the other hand, already had a lower CA of 38° compared to PEI membranes (Figure 7a,d). Initial ALD coating of 10 cycles resulted in a slight increase in CA, with additional cycles reducing it to 15−20° (Figure 7e).

To further investigate the change in the membrane's hydrophilicity after Al_2O_3 coating, we performed water permeability measurements while varying the number of ALD cycles of the membranes (Figure 7f,g). Both pristine membranes showed high water permeability (∼560 LMH/bar for PEI, ∼800 LMH/bar for PAN), which decreased with the increasing number of Al_2O_3 ALD cycles. This reduction is due to the decrease in pore size and membrane porosity (Figures 6a and S1) with Al_2O_3 deposition on the pore walls, in agreement with previous studies on ALD modified mem branes.[25,27,35] However, the growth of Al_2O_3 on the membranes changes not only the pore diameter but also the pore surface chemistry, from a pristine polymer surface to a heterogeneous polymer–Al_2O_3 surface and, with increasing cycles, to a pure Al_2O_3 surface. To better understand the contribution of the pore surface chemistry, we compared the pore diameter as measured by SEM image analysis and the pore diameter calculated from water permeability measure ments using the Hagen−Poiseuille equation for tortuous pores (eq 2, Table 2). The calculated pore diameter is higher than the measured one in all of the membranes. Interestingly, in PAN membranes, the calculated pore diameter increased from 57.1 nm for the pristine membrane to 68.0 nm after 10 ALD
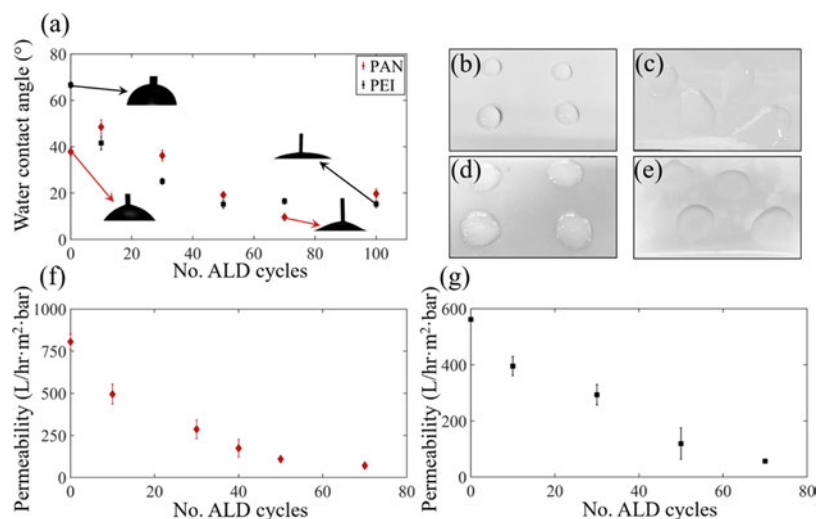

Figure 7. Effect of Al_2O_3 ALD on membrane surface wettability: (a) water contact angle measurement of PEI and PAN membranes after Al_2O_3 ALD with varying number of cycles. Water droplets on PEI (b, c) and PAN (d, e) membranes: (b, d) pristine membranes and (c, e) after 50 cycles of Al_2O_3 ALD. Water permeability measurements of (f) PAN and (g) PEI membranes with Al_2O_3 ALD surface modification.

Table 2. Comparison between Pore Diameters Measured by SEM Imaging and Calculated from Permeability Measurements

	PAN membrane		PEI membrane	
no. of ALD cycles	pore diameter (nm)[a]	pore diameter (nm)[b]	pore diameter (nm)[a]	pore diameter (nm)[b]
0	16.3 ± 37	57.1	20.6 ± 10.6	48.4
10	12.0 ± 3.8	68.0	19.3 ± 11.0	41.4
30	11.8 ± 1.7	64.0	15.6 ± 10.3	42.6
50	10.6 ± 1.4	53.3	14.1 ± 8.4	29.7
70	10.4 ± 1.2	57.2	12.4 ± 7.8	34.2

[a]Average pore diameter measured from SEM image analysis.
[b]Average pore diameter calculated from the measured water permeability using the Hagen−Poiseuille equation for tortuous pores.

cycles and was slightly reduced to 64.0 nm after 30 ALD cycles. This increase suggests that although the physical pore diameter and the membrane porosity were reduced with Al_2O_3 deposition, the addition of Al_2O_3 to the pore surface increased the membrane hydrophilicity, possibly enhancing the water permeability, relative to the reduced pore size. Additional ALD cycles on PAN membranes resulted in a decrease in the calculated pore diameter, as can be expected. The effect of Al_2O_3 layer on PAN membrane hydrophilicity at a low cycle number (<30) showed opposite trends through CA and permeability characterization and needs to be further investigated. In PEI membranes, the initial deposition of 10 cycles reduced the calculated pore size, but a slight increase in the calculated pore size was observed with 30 Al_2O_3 ALD cycles, indicating that a higher number of cycles is needed in PEI membranes to create an Al_2O_3 surface, which will improve the relative permeability.

3.4. Antifouling Performance. To probe the effect of Al_2O_3 ALD on oil antifouling, we performed fouling experiments with *in situ* imaging and examined the surface oil coverage as well as the increased pressure required to drive a constant flux through the membrane (Figures 8 and 9). For each membrane, we characterized the deposition of oil droplets (during the time period 0−20 min), followed by membrane

cleaning using crossflow with no permeation (time period: 25−40 min). Each data point in the graph represents an average of three experiments repeated with a new membrane coupon. Confocal microscopy was used to track the oil coverage on the membranes' surface. The surface coverage was extracted from the projection of three dimensional (3D) oil droplets on the membrane and calculated as the ratio of the surface covered with droplets (obtained *via* image analysis, Figure S5) to the total membrane area imaged. Three dimensional images of the "cleaned" membrane were acquired after 10 min of crossflow. The transmembrane pressure (TMP) is shown scaled against the initial value, corresponding to the TMP required to drive the imposed flux through a clean membrane. To confirm the total rejection of oil by the membrane, gas chromatography−mass spectrometry (GC MS) was used to detect oil in the feed and permeate (Figure S6).

Our analysis, shown in Figure 8, demonstrates that the PAN−Al_2O_3 membrane had lower surface coverage compared to the pristine PAN membrane, while the pressure required to sustain the permeate flux was almost equal. The lower surface coverage indicates that the Al_2O_3 coating can reduce oil accumulation on the surface. Following crossflow cleaning, the surface coverage was reduced from 73% and 92% to ∼30% for both PAN−Al_2O_3 and PAN, respectively, indicating that the attachment of oil droplets to the surface was similar for both surfaces.

Figure 9 presents similar trends of surface coverage and pressure demand for both PEI and PEI−Al_2O_3 surfaces. After crossflow cleaning, the surface coverage was reduced from ∼80% to ∼30% for both PEI and PEI−Al_2O_3. These results emphasize two significant properties of the Al_2O_3 modified PEI and PAN membranes: first, reduced oil surface coverage can allow for efficient membrane operation even under fouling conditions. Second, oil droplets can be easily removed from Al_2O_3 modified membranes using a simple physical cleaning mechanism. Thus, both membranes are good candidates for emulsion separation, even when challenged with high permeation flux. These outcomes correspond to the improved hydrophilicity and permeability results discussed in the previous sections. We anticipate that with further engineering
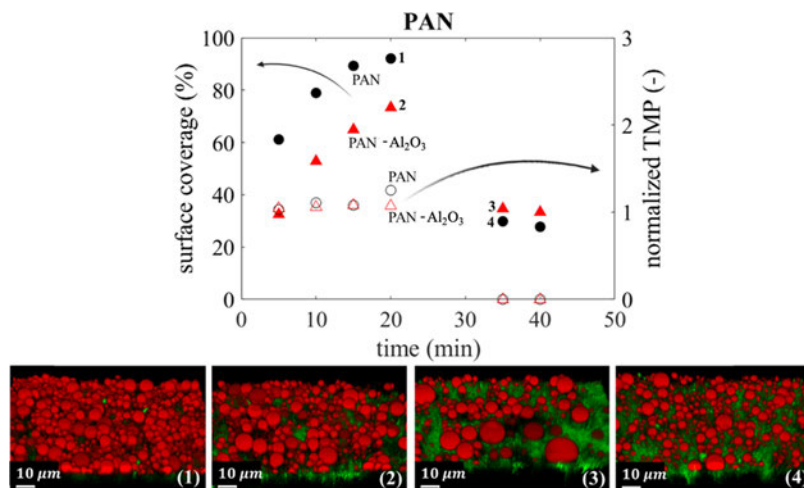

Figure 8. Top: membrane surface coverage and normalized TMP (TMP/TMP$_0$); PAN *vs* PAN−Al_2O_3 membrane performance at 300 LMH (PAN surface coverage, filled black dots; PAN−Al_2O_3 surface coverage, filled red triangles; PAN normalized TMP, empty black dots; and PAN−Al_2O_3 normalized TMP, empty red triangles). Bottom: confocal 3D reconstruction images of the membrane surface at representative times: red, oil droplets; green, membrane surface.
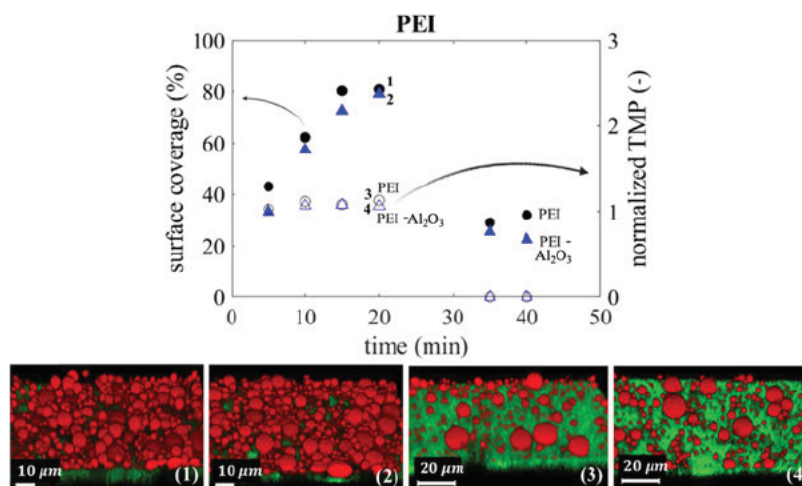
Figure 9. Top: droplet surface coverage and normalized TMP (TMP/TMP_0); PEI *vs* PEI–Al_2O_3 membrane performance at 300 LMH (PEI surface coverage, filled black dots; PEI–Al_2O_3 surface coverage, filled blue triangles; PEI normalized TMP, empty black dots; and PEI–Al_2O_3 normalized TMP, empty blue triangles). Bottom: confocal microscopy of the membrane surface at representative times: red, oil droplets; green, membrane surface.

of oxide composition, oxides with tightly bonded hydration layers, such as TiO_2 and SnO_2,[37] can achieve even higher oil antifouling behavior.

4. CONCLUSIONS

We have demonstrated membrane surface modification *via* Al_2O_3 ALD on two UF phase inverted membranes, PEI and PAN, and utilized the ease of growth on their surfaces to study gradient formation in UF polymeric membranes. We have shown, through TEM imaging and EDS analysis, that Al_2O_3 growth gradient through the depth of the membrane can be controlled *via* tuning the precursors' exposure time. At short exposure times, there is an excess of Al_2O_3 at the top of the membrane, creating pore blockage, while in longer exposure times, this phenomenon is reduced. The Al_2O_3 growth increases the hydrophilicity of PEI and PAN membranes due to the creation of a hydrophilic oxide interface. While extensive growth reduces the pore size and hence overall permeability, moderate growth of 10–30 cycles can enable precise tuning and optimization of the membrane properties. Both modified membranes showed reduced oil coverage during oil–water emulsion separation and good fouling removal upon crossflow cleaning. Better understanding of gradient formation in ALD membrane surface modification and the effect of oxide interface on membrane permeability and fouling will enable better design of these composite membranes.

AUTHOR INFORMATION

Corresponding Author

Tamar Segal Peretz − *Department of Chemical Engineering, Technion—Israel Institute of Technology, Haifa 3200003, Israel;* orcid.org/0000 0003 3222 6429; Email: tamarps@technion.ac.il

Authors

Tamar Itzhak − *Department of Chemical Engineering, Technion—Israel Institute of Technology, Haifa 3200003, Israel*

Naama Segev Mark − *Department of Civil and Environmental Engineering, Technion—Israel Institute of Technology, Haifa 32000, Israel*

Assaf Simon − *Department of Chemical Engineering, Technion—Israel Institute of Technology, Haifa 3200003, Israel*

Volker Abetz − *Institute of Membrane Research, Helmholtz Zentrum Geesthacht, 21502 Geesthacht, Germany; Institute of Physical Chemistry, Universität Hamburg, 20146 Hamburg, Germany;* orcid.org/0000 0002 4840 6611

Guy Z. Ramon − *Department of Civil and Environmental Engineering, Technion—Israel Institute of Technology, Haifa 32000, Israel;* orcid.org/0000 0002 0711 0654

Notes

The authors declare no competing financial interest.

REFERENCES

(1) Rana, D.; Matsuura, T. Surface Modifications for Antifouling Membranes. *Chem. Rev.* **2010**, *110*, 2448−2471.

(2) Ulbricht, M. Advanced Functional Polymer Membranes. *Polymer* **2006**, *47*, 2217−2262.

(3) Khulbe, K. C.; Feng, C.; Matsuura, T. The Art of Surface Modification of Synthetic Polymeric Membranes. *J. Appl. Polym. Sci.* **2010**, *115*, 855−895.

(4) Asatekin, A.; Kang, S.; Elimelech, M.; Mayes, A. M. Anti Fouling Ultrafiltration Membranes Containing Polyacrylonitrile Graft Poly

(Ethylene Oxide) Comb Copolymer Additives. *J. Membr. Sci.* **2007**, *298*, 136−146.

(5) Ma, X.; Su, Y.; Sun, Q.; Wang, Y.; Jiang, Z. Enhancing the Antifouling Property of Polyethersulfone Ultrafiltration Membranes through Surface Adsorption Crosslinking of Poly(Vinyl Alcohol). *J. Membr. Sci.* **2007**, *300*, 71−78.

(6) Xie, Y.; Yu, H.; Wang, S.; Xu, Z. Improvement of Antifouling Characteristics in a Bioreactor of Polypropylene Microporous Membrane by the Adsorption of Tween 20. *J. Environ. Sci.* **2007**, *19*, 1461−1465.

(7) Wang, Y. Q.; Su, Y. L.; Ma, X. L.; Sun, Q.; Jiang, Z. Y. Pluronic Polymers and Polyethersulfone Blend Membranes with Improved Fouling Resistant Ability and Ultrafiltration Performance. *J. Membr. Sci.* **2006**, *283*, 440−447.

(8) Reddy, A. V. R.; Mohan, D. J.; Bhattacharya, A.; Shah, V. J.; Ghosh, P. K. Surface Modification of Ultrafiltration Membranes by Preadsorption of a Negatively Charged Polymer: I. Permeation of Water Soluble Polymers and Inorganic Salt Solutions and Fouling Resistance Properties. *J. Membr. Sci.* **2003**, *214*, 211−221.

(9) Reddy, A. V. R.; Patel, H. R. Chemically Treated Polyethersulfone/Polyacrylonitrile Blend Ultrafiltration Membranes for Better Fouling Resistance. *Desalination* **2008**, *221*, 318−323.

(10) González Muñoz, M. P.; Navarro, R.; Saucedo, I.; Avila, M.; Prádanos, P.; Palacio, L.; Martínez, F.; Martín, A.; Hernández, A. Hydrofluoric Acid Treatment for Improved Performance of a Nanofiltration Membrane. *Desalination* **2006**, *191*, 273−278.

(11) He, X. C.; et al. Reducing protein fouling of a polypropylene microporous membrane by CO_2 plasma surface modification. *Desalination* **2020**, 80−89.

(12) Lohokare, H. R.; Kumbharkar, S. C.; Bhole, Y. S.; Kharul, U. K. Surface Modification of Polyacrylonitrile Based Ultrafiltration Membrane. *J. Appl. Polym. Sci.* **2006**, *101*, 4378−4385.

(13) Gu, J. S.; Yu, H. Y.; Huang, L.; Tang, Z. Q.; Li, W.; Zhou, J.; Yan, M. G.; Wei, X. W. Chain Length Dependence of the Antifouling Characteristics of the Glycopolymer Modified Polypropylene Membrane in an SMBR. *J. Membr. Sci.* **2009**, *326*, 145−152.

(14) Xu, Q.; Yang, J.; Dai, J.; Yang, Y.; Chen, X.; Wang, Y. Hydrophilization of Porous Polypropylene Membranes by Atomic Layer Deposition of TiO2 for Simultaneously Improved Permeability and Selectivity. *J. Membr. Sci.* **2013**, *448*, 215−222.

(15) Du, J. R.; Peldszus, S.; Huck, P. M.; Feng, X. Modification of Poly(Vinylidene Fluoride) Ultrafiltration Membranes with Poly(Vinyl Alcohol) for Fouling Control in Drinking Water Treatment. *Water Res.* **2009**, *43*, 4559−4568.

(16) Boributh, S.; Chanachai, A.; Jiraratananon, R. Modification of PVDF Membrane by Chitosan Solution for Reducing Protein Fouling. *J. Membr. Sci.* **2009**, *342*, 97−104.

(17) Chang, Y.; Ko, C. Y.; Shih, Y. J.; Quémener, D.; Deratani, A.; Wei, T. C.; Wang, D. M.; Lai, J. Y. Surface Grafting Control of PEGylated Poly(Vinylidene Fluoride) Antifouling Membrane via Surface Initiated Radical Graft Copolymerization. *J. Membr. Sci.* **2009**, *345*, 160−169.

(18) Boo, C.; Lee, J.; Elimelech, M. Omniphobic Polyvinylidene Fluoride (PVDF) Membrane for Desalination of Shale Gas Produced Water by Membrane Distillation. *Environ. Sci. Technol.* **2016**, *50*, 12275−12282.

(19) Wu, S. L.; Liu, F.; Yang, H. C.; Darling, S. B. Recent Progress in Molecular Engineering to Tailor Organic−Inorganic Interfaces in Composite Membranes. *Mol. Syst. Des. Eng.* **2020**, *5*, 433−444.

(20) Yang, H. C.; Waldman, R. Z.; Chen, Z.; Darling, S. B. Atomic Layer Deposition for Membrane Interface Engineering. *Nanoscale* **2018**, *10*, 20505−20513.

(21) Weber, M.; Julbe, A.; Kim, S. S.; Bechelany, M. Atomic Layer Deposition (ALD) on Inorganic or Polymeric Membranes. *J. Appl. Phys.* **2019**, *126*, No. 041101.

(22) Juholin, P.; Kääriäinen, M. L.; Riihimäki, M.; Sliz, R.; Aguirre, J. L.; Pirilä, M.; Fabritius, T.; Cameron, D.; Keiski, R. L. Comparison of ALD Coated Nanofiltration Membranes to Unmodified Commercial Membranes in Mine Wastewater Treatment. *Sep. Purif. Technol.* **2018**, *192*, 69−77.

(23) Lee, A.; Libera, J. A.; Waldman, R. Z.; Ahmed, A.; Avila, J. R.; Elam, J. W.; Darling, S. B. Conformal Nitrogen Doped TiO2 Photocatalytic Coatings for Sunlight Activated Membranes. *Adv. Sustainable Syst.* **2017**, *1*, No. 1600041.

(24) Li, N.; Zhang, J.; Tian, Y.; Zhang, J.; Zhan, W.; Zhao, J.; Ding, Y.; Zuo, W. Hydrophilic Modification of Polyvinylidene Fluoride Membranes by ZnO Atomic Layer Deposition Using Nitrogen Dioxide/Diethylzinc Functionalization. *J. Membr. Sci.* **2016**, *514*, 241−249.

(25) Xu, Q.; Yang, Y.; Wang, X.; Wang, Z.; Jin, W.; Huang, J.; Wang, Y. Atomic Layer Deposition of Alumina on Porous Polytetrafluoro ethylene Membranes for Enhanced Hydrophilicity and Separation Performances. *J. Membr. Sci.* **2012**, *415−416*, 435−443.

(26) Yang, W.; Son, M.; Rossi, R.; Vrouwenvelder, J. S.; Logan, B. E. Adapting Aluminum Doped Zinc Oxide for Electrically Conductive Membranes Fabricated by Atomic Layer Deposition. *ACS Appl. Mater. Interfaces* **2020**, *12*, 963−969.

(27) Li, F.; Li, L.; Liao, X.; Wang, Y. Precise Pore Size Tuning and Surface Modifications of Polymeric Membranes Using the Atomic Layer Deposition Technique. *J. Membr. Sci.* **2011**, *385−386*, 1−9.

(28) Wang, H.; Wei, M.; Zhong, Z.; Wang, Y. Atomic Layer Deposition Enabled Thin Film Composite Membranes of Polyimide Supported on Nanoporous Anodized Alumina. *J. Membr. Sci.* **2017**, *535*, 56−62.

(29) Johnson, R. W.; Hultqvist, A.; Bent, S. F. A Brief Review of Atomic Layer Deposition: From Fundamentals to Applications. *Mater. Today* **2014**, *17*, 236−246.

(30) Wang, Q.; Wang, X.; Wang, Z.; Huang, J.; Wang, Y. PVDF Membranes with Simultaneously Enhanced Permeability and Selectivity by Breaking the Tradeoff Effect via Atomic Layer Deposition of TiO2. *J. Membr. Sci.* **2013**, *442*, 57−64.

(31) Zhou, X.; Zhao, Y. Y.; Kim, S. R.; Elimelech, M.; Hu, S.; Kim, J. H. Controlled TiO_2 Growth on Reverse Osmosis and Nano filtration Membranes by Atomic Layer Deposition: Mechanisms and Potential Applications. *Environ. Sci. Technol.* **2018**, *52*, 14311−14320.

(32) Alam, J.; Alhoshan, M.; Dass, L. A.; Shukla, A. K.; Muthumareeswaran, M. R.; Hussain, M.; Aldwayyan, A. S. Atomic Layer Deposition of TiO2 Film on a Polyethersulfone Membrane: Separation Applications. *J. Polym. Res.* **2016**, *23*, No. 183.

(33) Sheng, T.; Chen, H.; Xiong, S.; Chen, X.; Wang, Y. Atomic Layer Deposition of Polyimide on Microporous Polyethersulfone Membranes for Enhanced and Tunable Performances. *AIChE J.* **2014**, *60*, 3614−3622.

(34) Zhou, C.; Segal Peretz, T.; Oruc, M. E.; Suh, H. S.; Wu, G.; Nealey, P. F. Fabrication of Nanoporous Alumina Ultrafiltration Membrane with Tunable Pore Size Using Block Copolymer Templates. *Adv. Funct. Mater.* **2017**, *27*, No. 1701756.

(35) Waldman, R. Z.; Yang, H. C.; Mandia, D. J.; Nealey, P. F.; Elam, J. W.; Darling, S. B. Janus Membranes via Diffusion Controlled Atomic Layer Deposition. *Adv. Mater. Interfaces* **2018**, *5*, No. 1800658.

(36) Jia, X.; Low, Z.; Chen, H.; Xiong, S.; Wang, Y. Atomic Layer Deposition of Al2O3 on Porous Polypropylene Hollow Fibers for Enhanced Membrane Performances. *Chin. J. Chem. Eng.* **2018**, *26*, 695−700.

(37) Yang, H. C.; Xie, Y.; Chan, H.; Narayanan, B.; Chen, L.; Waldman, R. Z.; Sankaranarayanan, S. K. R. S.; Elam, J. W.; Darling, S. B. Crude Oil Repellent Membranes by Atomic Layer Deposition: Oxide Interface Engineering. *ACS Nano* **2018**, *12*, 8678−8685.

(38) Yang, X.; Sun, P.; Zhang, H.; Xia, Z.; Waldman, R. Z.; Mane, A. U.; Elam, J. W.; Shao, L.; Darling, S. B. Polyphenol Sensitized Atomic Layer Deposition for Membrane Interface Hydrophilization. *Adv. Funct. Mater.* **2020**, *30*, No. 1910062.

(39) Rabbani, A.; Jamshidi, S.; Salehi, S. An Automated Simple Algorithm for Realistic Pore Network Extraction from Micro Tomography Images. *J. Pet. Sci. Eng.* **2014**, *123*, 164−171.

(40) Bason, S.; Freger, V. Phenomenological Analysis of Transport of Mono and Divalent Ions in Nanofiltration. *J. Membr. Sci.* **2010**, *360*, 389−396.

(41) Bason, S.; et al. Analysis of Ion Transport in Nanofiltration Using Phenomenological Coefficients and Structural Characteristics. *J. Phys. Chem. B* **2020**, 3510−3517.

(42) Yachnin, E.; Ramon, G. Z. Direct Observation of Macro molecular Deposition on a Nanofiltration Membrane. *Sep. Sci. Technol.* **2017**, *52*, 258−265.

(43) Vu, A.; Mark, N. S.; Ramon, G. Z.; Qian, X.; Sengupta, A.; Wickramasinghe, S. R. Oil Deposition on Polymer Brush Coated NF Membranes. *Membranes* **2019**, *9*, No. 168.

(44) Fux, G.; Ramon, G. Z. Microscale Dynamics of Oil Droplets at a Membrane Surface: Deformation, Reversibility, and Implications for Fouling. *Environ. Sci. Technol.* **2017**, *51*, 13842−13849.

(45) Alam, J.; Alam, J.; Kumar Shukla, A.; Alhoshan, M.; Khaled, J. M.; Al Masry, W. A.; Alharbi, N. S.; Alam, M. Graphene Oxide Silver Nanosheet Incorporated Polyamide Thin Film Composite Mem branes for Antifouling and Antibacterial Action against Escherichia Coli and Bovine Serum Albumin. *J. Ind. Eng. Chem.* **2019**, *80*, 227−238.

(46) Lin, Y. M.; Song, C.; Rutledge, G. C. Direct Three Dimensional Visualization of Membrane Fouling by Confocal Laser Scanning Microscopy. *ACS Appl. Mater. Interfaces* **2019**, *11*, 17001−17008.

(47) Segev Mark, N.; Vu, A.; Chen, N.; Qian, X.; Wickramasinghe, S. R.; Ramon, G. Z. Colloidal Deposition on Polymer Brush Coated NF Membranes. *Sep. Purif. Technol.* **2019**, *219*, 208−215.

(48) Elam, J. W.; Routkevitch, D.; Mardilovich, P. P.; George, S. M. Conformal Coating on Ultrahigh Aspect Ratio Nanopores of Anodic Alumina by Atomic Layer Deposition. *Chem. Mater.* **2003**, *15*, 3507−3517.

(49) Zazpe, R.; Knaut, M.; Sopha, H.; Hromadko, L.; Albert, M.; Prikryl, J.; Gärtnerová, V.; Bartha, J. W.; Macak, J. M. Atomic Layer Deposition for Coating of High Aspect Ratio TiO2 Nanotube Layers. *Langmuir* **2016**, *32*, 10551−10558.